The effect of surface gravity waves on the measurement of river surface velocity

G. Dolcetti
The University of Sheffield, Sheffield, United Kingdom

B. Hortobágyi, M. Perks
Newcastle University, Newcastle, United Kingdom

S.J. Tait
The University of Sheffield, Sheffield, United Kingdom

ABSTRACT: Optical methods are increasingly used as a means to determine the flow velocity at the surface of rivers. If applied in the absence of visible physical tracers (e.g., floating debris), current methods must rely on the assumption that the water surface deformations are directly advected by the river flow. This assumption is weak in the presence of gravity waves, which propagate in various directions at their own speed. To investigate the properties and effects of these waves, we record videos of a small, shallow river, in the absence of significant wind. Using the image intensity as a proxy for the surface elevation, we demonstrate the presence of gravity waves on the free surface by means of a space-time Fourier analysis. The dominant wavelength in all directions closely matches the wavelength of stationary waves with the front perpendicular to the flow direction. This observation is in accordance with previous laboratory studies. This suggests that the waves originate from the interaction of the flow with the rough bed, and that they are a feature of shallow flows over rough beds. Characteristic ring-wave patterns emerge in the space-time correlation. They are related with a periodic fluctuation of the peak correlation, usually associated with the mean surface velocity. The effect will impact on standard optical surface velocimetry methods if applied to flows without visible floating tracers, but knowledge of gravity waves dynamics can be exploited to infer time averaged characteristics of the river flow.

1 INTRODUCTION

Non-contact velocity measurement techniques typically estimate the velocity of a river flow near the free surface by tracking the motion of one or more features. Such features can be surface deformations or visible floating tracers that are intentionally or unintentionally distributed at or near the surface, and are assumed to be passively transported by the flow. Video-based methods, and in particular the Large Scale Particle Image Velocimetry (LSPIV) method (e.g. Muste et al. 2008), seem to be very strongly affected by the density and homogeneity of the seeding distribution (Tauro et al. 2014). At low seeding densities, the image intensity distribution is mainly produced by ambient light scattered by the rough water surface. As long as the free surface deformations are rigidly advected by the flow, the accuracy of the method should be assured. In reality, the dynamics of the free surface of turbulent flows are more complex. Gravity-capillary waves that propagate in different directions with a wavelength-dependent celerity can coexist with rigidly advected deformations (Savelsberg & van de Water 2009, Dolcetti et al. 2016). The presence of surface gravity waves, and especially of stationary (or standing) waves, appears to be associated with the underestimation of the surface velocity predicted by LSPIV methods when seeding density is low (Tauro et al. 2014, Benetazzo et al. 2017).

The aim of this study was to identify the presence of gravity waves at the surface of a shallow river, and to observe their effects on the spatio-temporal image correlation, in the absence of floating tracers. The spatio-temporal correlation is the basis of velocity estimates using LSPIV.

Videos of a shallow river have been collected using a low-cost camera, and the corresponding image intensity distributions have been subjected to a three-dimensional Fourier analysis to identify the nature of the surface fluctuations. A simplified analytic model of the correlation function of the free surface of shallow flows has been derived, and compared with this analysis. The effects on correlation-based velocimetry methods such as LSPIV has been investigated based on a simplified LSPIV algorithm, and a new alternative velocity estimation procedure has been proposed based on a more in-depth understanding of the water surface fluctuations that removes the need for numerous floating tracers.

2 CORRELATION FUNCTION OF GRAVITY WAVES IN A SHALLOW FLOW

Laboratory experiments have revealed the coexistence of two main types of surface deformations at the free surface of shallow turbulent flows: gravity-capillary waves that propagate relative to the mean flow with a wavelength-dependent celerity, and deformations that move along with the flow and are presumably generated by turbulence (Savelesberg & van de Water 2009, Dolcetti et al. 2016). These two types of deformation can be distinguished by means of a frequency-wavenumber Fourier analysis applied to spatio-temporal data. This analysis identifies the relation between the frequency f (sometimes expressed as $\omega = 2\pi f$) and the wavelength λ (or the corresponding wavenumber $k = 2\pi/\lambda$) of each mode of the surface elevation data. For the rigidly advected modes, the expected relation is

$$\omega(\mathbf{k}) = \mathbf{k} \cdot \mathbf{U}, \tag{1}$$

where $\mathbf{U}$ is the flow velocity vector. Gravity-capillary waves in still water have the intrinsic frequency

$$\omega_0(k) = \sqrt{(gk + \gamma k^3/\rho)\tanh(kd)}, \tag{2}$$

where g is the acceleration due to gravity, γ is the surface tension coefficient, ρ is the water density, and d is the water depth. In the presence of a current, the waves move with respect to the mean flow with a celerity ω_0/k that depends on the wavenumber k. The resulting dispersion relation is

$$\omega(\mathbf{k}) = \mathbf{k} \cdot \mathbf{U} \pm \omega_0(k). \tag{3}$$

In a laboratory flume with a rough bed, Dolcetti et al. (2016) found that the horizontal scale of the surface elevation scaled consistently with the wavelength $\lambda_0 = 2\pi/k_0$, where k_0 is the wavenumber for which $\omega(\mathbf{k}_0) = 0$ when $\mathbf{k}_0 \cdot \mathbf{U} = -k_0 U$. From Equation (3),

$$k_0 = \omega_0(k_0)/U, \tag{4}$$

which can be solved numerically if U is larger than the minimum gravity wave celerity ≈ 0.23 m/s. The celerity of a wave with wavenumber k_0 equals the speed of the flow. If such a wave is directed against the current, it appears to remain static (stationary wave). If, instead, it propagates in any other direction, its frequency is determined by Equation (3) and it is $\omega \neq 0$. If the flow is sufficiently deep ($kd > 1$, $\rho g d^2/\gamma \gg 1$), then

$$k_0 \approx g/U^2. \tag{5}$$

According to Wiener-Khinchin's theorem, the correlation function W of a statistically stationary signal equals the inverse cosine transform of its Fourier power spectrum ψ,

$$W(\mathbf{r}, \tau) = \int_{-\pi}^{\pi} \int_0^\infty \psi(k, \theta) \cos\left[\mathbf{k} \cdot \mathbf{r} - \omega(k, \theta)\tau\right] \mathrm{d}k\mathrm{d}\theta, \tag{6}$$

where θ indicates the angle of propagation of the waves with respect to the flow direction. Dolcetti & García Nava (2019) noted that the waves with wavenumber k_0 tend to dominate the spectrum in every direction, and proposed to simplify the representation neglecting all waves with a different wavenumber, introducing

$$\psi(k, \theta) = \chi(\theta)\delta(k - k_0), \tag{7}$$

where δ is a delta function, and χ is called an angular spreading function. This resulted in

$$W(\mathbf{r}, \tau) = \int_{-\pi}^{\pi} \chi(\theta) \cos\left[\mathbf{k}_0 \cdot (\mathbf{r} - \mathbf{U}\tau) - \omega_0(k_0)\tau\right] \mathrm{d}\theta. \tag{8}$$

Although Equation (8) neglects the presence of other types of waves (including any rigidly advected surface deformations), it is able to explain the oscillation like $\cos\left[\omega_0(k_0)\tau\right]$ of the correlation function along the path $\mathbf{r} = \mathbf{U}\tau$ observed in earlier laboratory experiments (Horoshenkov et al. 2013), as demonstrated by Dolcetti & García Nava (2019).

Particle Image Velocimetry methods are based on a cross-correlation between images taken at different times (Muste et al. 2008). Although there are variations in the algorithms used, and the resolution of the method is often improved by means of spatial interpolations, the fundamental principle is simple. For a given time interval τ, the velocity is calculated as $\mathbf{U} = \mathbf{r}_W/\tau$, where $\mathbf{r}_W$ is the location $\mathbf{r}$ of the maximum of the correlation $W(\mathbf{r}, \tau)$. If the density of seeding material is scarce and the illumination intensity fairly uniform, the image light intensity distribution is expected to be dominated by the modulation of the reflected ambient light by the water waves and ripples. In these conditions, the Fourier spectra and correlations of the images are related to those of the surface slope, which in turn are directly related to the spectra and correlations of the surface elevation (Lubard et al. 1980). Then, the periodic fluctuation of the surface correlation at the point $\mathbf{r} = \mathbf{U}\tau$ caused by gravity waves may affect the performance of LSPIV methods especially at large τ, or low frame rates.

To quantify these effects, it is necessary to calculate the whole correlation function $W(\mathbf{r}, \tau)$, which depends on the angular spreading function $\chi(\theta)$. Assuming $\chi(\theta)$ to have a cosine-series representation,

$$\chi(\theta) = \frac{a_0}{2} + \sum_{n=1}^{\infty} a_n \cos(n\theta), \tag{9}$$

where

$$a_n = \frac{1}{\pi}\int_{-\pi}^{\pi}\chi(\theta)\cos(n\theta)\mathrm{d}\theta, \tag{10}$$

then, from Equation (8),

$$W(\mathbf{r}, \tau) = \pi a_0 \mathrm{J}_0(k_0|\mathbf{r} - \mathbf{U}\tau|)\cos\left[\omega_0(k_0)\tau\right] +$$

$$+\pi\sum_{n=1}^{\infty} a_n(-1)^{n/2}\cos(n\beta)\left[\mathrm{J}_n(k_0|\mathbf{r} - \mathbf{U}\tau|)e^{-\mathrm{i}\omega_0(k_0)\tau} + \mathrm{J}_n(-k_0|\mathbf{r} - \mathbf{U}\tau|)e^{\mathrm{i}\omega_0(k_0)\tau}\right], \tag{11}$$

where $\mathrm{i} = \sqrt{-1}$, J_n is the Bessel function of the first kind of order n, and β is the angle of vector $\mathbf{r} - \mathbf{U}\tau$ measured from the direction of $\mathbf{U}$. To represent the angular spreading function, Dolcetti & García Nava (2019) proposed the Von Mises distribution

$$\chi(\theta) = \exp\left\{-b\left[\cos(\theta) + 1\right]\right\}, \tag{12}$$

where b is a spreading parameter which was found to be between 1 and 2. Equation (12) has its maximum at $\theta = \pm\pi$, for the waves directed against $\mathbf{U}$. Substituting in Equation 10,

$$a_n = 2e^{-b}\mathrm{I}_n(-b), \tag{13}$$

where I_n is the modified Bessel function of the first kind of order n. For this specific function,

$$W(\mathbf{r}, \tau) = 2\pi e^{-b}\mathrm{I}_0(-b)\mathrm{J}_0(k_0|\mathbf{r} - \mathbf{U}\tau|)\cos(\omega_0\tau) +$$

$$+2\pi e^{-b}\sum_{n=1}^{\infty}\mathrm{I}_n(-b)(-1)^{n/2}\cos(n\beta)\left[\mathrm{J}_n(k_0|\mathbf{r} - \mathbf{U}\tau|)e^{-\mathrm{i}\omega_0(k_0)\tau} + \mathrm{J}_n(-k_0|\mathbf{r} - \mathbf{U}\tau|)e^{\mathrm{i}\omega_0(k_0)\tau}\right]. \tag{14}$$

In the following sections, Equation (14) is compared with the measured correlation of images of a river surface, to identify more clearly the effects of the gravity waves with wavenumber k_0 on LSPIV-based spatial correlations. All calculations were performed with $b = 2$, considering the first 10 terms of the series. The correlation function was normalised to give $W(\mathbf{0}, 0) = 1$.

3 DATA COLLECTION

The measurement was performed on the River Sheaf in Sheffield, United Kingdom (Latitude: 53.373056° Longitude: -1.463913° (WGS 84)). In the measured section, the river is flowing
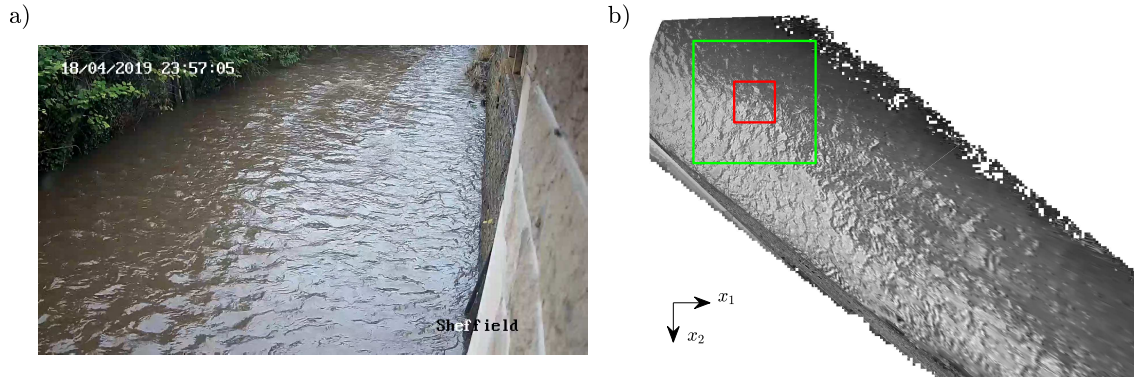
Figure 1. (a) Example of a single video frame. The flow is from top-right to bottom-left. (b) Example of rectified image. The flow is from bottom-right to top-left after rectification. The squares indicate the part of image effectively used for the analysis. A different area was used (green) for the spectral analysis (6×6 m), and (red) for the correlation analysis (2×2 m), to optimise the visualisation of results.

through an urban area, and is heavily modified. The river is approximately straight with a trapezoidal cross-section, and has a width of 9.2 m at the water surface. The bed is covered with large gravel and appeared stable. A sharp-crested calibrated measurement weir is located approximately 25 m downstream of the measurement section and is used by the UK Environment Agency to monitor flow rates and stage at this location.

For this study, a 5 minute long video recording of the River Sheaf was used. The video was recorded with a fixed low-cost camera (Hikvision DS-2CD2T42WD-I8 6mm IP camera), at a resolution of 1920×1080 pixels, and with a frame rate of 20 fps. The camera was installed at a height of 4.5 m from the water surface on the left channel wall, looking upstream at an oblique angle of approximately 30 degrees. An example of an image frame captured by the camera is shown in Figure 1a. The images were mapped to geographic coordinates using ground control points obtained from a high-resolution point cloud acquired with a Leica MS50 multi-station. An example of orthorectified image is shown in Figure 1b. The rectified images were defined on a regular grid with size of 0.02 m. Prior to the analysis, the data was debiased and normalised at each pixel. The images were analysed in groups of 200 consecutive frames (10 seconds), and the statistics (spectrum and correlation function) were averaged across 29 groups.

4 RESULTS

4.1 *Frequency-wavenumber spectra*

The average frequency-wavenumber spectrum was calculated by means of a three-dimensional Fourier analysis (2D in space, 1D in time) applied to the images. The analysis was limited to an area of the image with size 6×6 m (green square in Figure 1b). The size of the area was chosen in order to give the maximum achievable spectral resolution given the width of the river and the oblique orientation of the rectified images.

Four cross-sections of the 3D spectrum at different constant frequencies are shown in Figure 2. The straight (dash-dot) line represents Equation (1), while the two dashed curved lines indicate Equation (3) with the plus and minus term. The three dispersion relations are shifted progressively towards negative values of both wavenumber components (parallel to the velocity) with the increase of frequency, in accordance with Equation (1). Since both components of the flow velocity were negative, the waves with $k_1 < 0$ and $k_2 < 0$ were the ones that propagated along the flow, while those with $k_1 > 0$ and $k_2 > 0$ propagated against it. The amplitude of the measured spectra was higher in correspondence with the expected relations, indicating good agreement with the theory, although the waves on the bottom-left corner of the plots were slightly shifted towards the origin with respect to the theory. The amplitude of all waves appeared to decrease with the increase of frequency. The waves on the top-right part of the plots appeared to dominate at each frequency. At the time of measurement, the average river depth was 0.34 m, while the mean surface velocity was 1.1 m/s. The maximum frequency of the waves with wavenumber modulus k_0 was $2\omega_0(k_0)/2\pi = 2.8$ Hz, when they propagated along the current. Below this frequency,
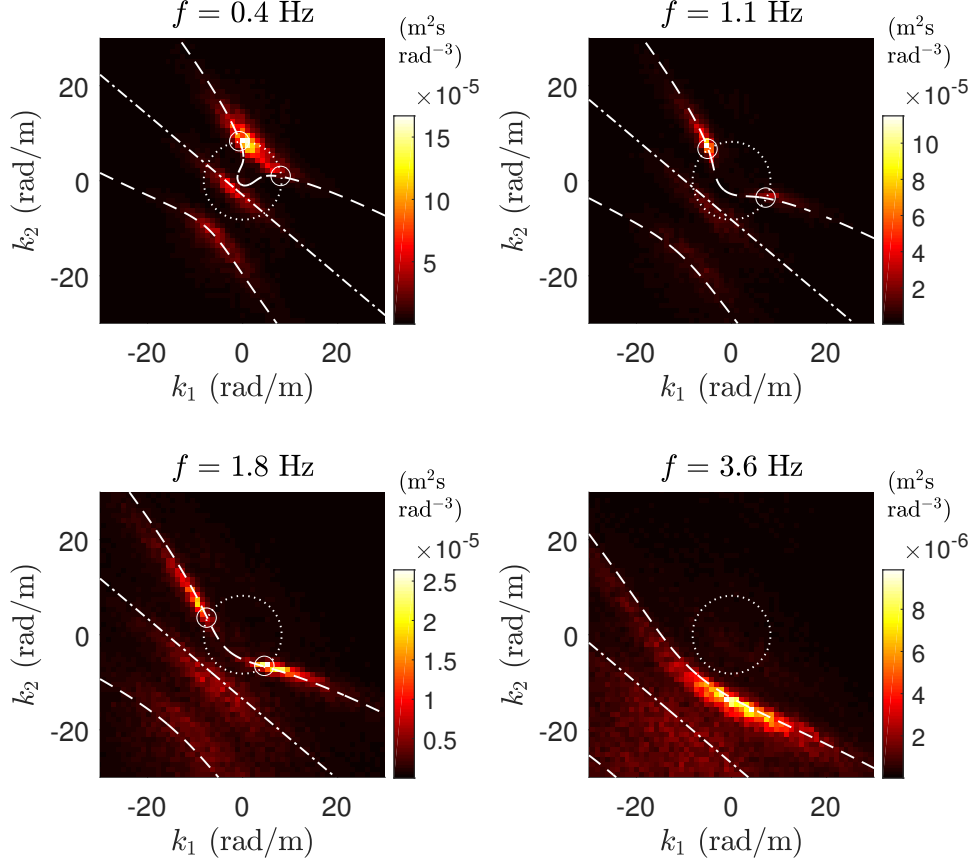
Figure 2. Constant-frequency sections through the average three-dimensional frequency-wavenumber spectrum of the video. The frequency is indicated at the top of each plot. k_1 and k_2 are the components of the wavenumber vector $\mathbf{k}$ in the directions x_1 and x_2, respectively. (dashed) Dispersion relation of gravity-capillary waves, Equation (4). (dashed-dotted) Rigidly advected features, Equation (3). (circle, dotted) Waves with the characteristic wavenumber modulus $|\mathbf{k}| = k_0$. (small circles, solid) Intersection of Equation (4) with $|\mathbf{k}| = k_0$, indicating gravity-capillary waves with $|\mathbf{k}| = k_0$.

Equation (3) and the circle with radius k_0 intersect, and the peaks of each section of the spectrum occurred at this intersection. The amplitude of rigidly advected features was found to be three times lower than these peaks. At 3.6 Hz, the spectrum was broader with a wider distribution of wavenumbers. The behaviour at low frequencies indicates the prevalence of the waves with wavenumber k_0, in accordance with previous studies by Dolcetti et al. (2016) and Dolcetti & García Nava (2019). This result confirms the relative importance of gravity waves, and the limited validity of the rigid advection assumption, for shallow flow surfaces in rivers.

4.2 *Spatio-temporal correlation*

The average spatio-temporal correlation functions were calculated using a smaller 2×2 m window (see Figure 1b, in red), since the correlation was found to decay rapidly beyond a 1 m spatial separation. Examples of the measured and expected average correlation are shown in Figure 3 and Figure 4, respectively. These figures show the behaviour of the correlation in space for various time separations between 0 s (image auto-correlation) and 1.25 s. The intrinsic frequency of the waves with wavenumber k_0 was $\omega_0(k_0)/2\pi = 1.42$ Hz, which corresponds to a characteristic period of 0.7 s. Each plot in Figure 3 and 4 is approximately a quarter of period apart. The asterisks in Figure 3 and 4 indicate the point $\mathbf{r} = \mathbf{U}\tau$. Focusing on the value of the correlation at this point, it is possible to observe its fluctuation from positive ($\tau = 0$ s) to negative ($\tau = 0.35$ s, half period), then to positive again ($\tau = 0.7$ s). At each time separation, the plots show a succession of peaks and troughs in space, with a wavelength of approximately $2\pi/k_0 = 0.77$ m.

The measured correlation in Figure 3 can be compared with the expected one calculated with Equation (14) and shown in Figure 4. The expected correlation also shows an oscillation with
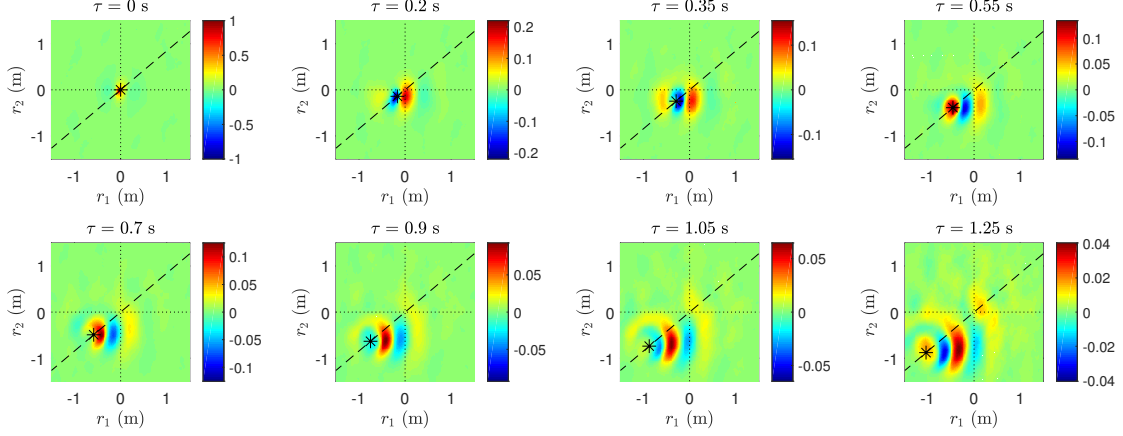
Figure 3. Measured spatio-temporal cross-correlation of the image intensity, $W(\mathbf{r}, \tau)$, for various time separations τ (indicated at the top of each plot). The characteristic period of the surface fluctuations was 0.7 s. The dashed line indicates the intersection with the plane parallel to the flow velocity, $\mathbf{r} \propto \mathbf{U}$, which is directed towards the bottom left. (asterisk) Expected peak of the correlation, assuming rigid advection, $\mathbf{r} = \mathbf{U}\tau$. The range of the color scale is $\pm \max\{|W(\mathbf{r}, \tau)|\}$, and is different for each sub-plot.
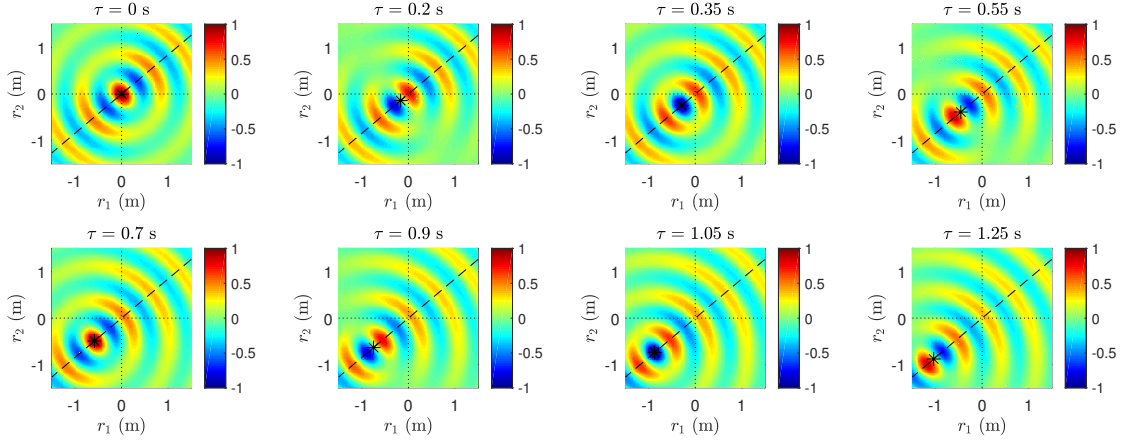

Figure 4. Model of the spatio-temporal cross-correlation based on Equation (14).

time at the point $\mathbf{r} = \mathbf{U}\tau$, with a period of 0.7 s. The peaks and troughs at each temporal separation τ are more easily discerned than in Figure 3, and take the shape of quasi-concentric circles, or ring-waves, with the origin at $\mathbf{r} = \mathbf{U}\tau$. These were caused by the Bessel functions in Equation (14). The resemblance between the measured and expected correlations suggests that both the temporal oscillation at $\mathbf{r} = \mathbf{U}\tau$ with frequency $\omega_0(k_0)$, and the concentric circles with wavelength $2\pi/k_0$, were caused by the gravity waves with wavenumber k_0. The amplitude of the measured correlation function in Figure 3 was found to decay much more rapidly both in space and in time than predicted by Equation (14). This was likely due to the presence of additional waves with wavenumber different from k_0 in the measurements, not accounted for by the simplified model.

4.3 *Velocity calculations*

A rigorous quantification of the uncertainty of LSPIV methods in unseeded flows would require considering state-of-the-art algorithms, which include filtering and interpolations to improve robustness of the method. This is beyond the scope of this work. As an indication of the potential effects of waves on the accuracy of these methods, we propose to use a simplified LSPIV algorithm. Figure 5a and 5b show the sections of the measured and modelled correlation function, respectively, through the plane parallel to the flow velocity $\mathbf{U}$ (i.e. $\mathbf{r} = \rho \mathbf{U}/U$, with ρ a real variable). The plane is indicated with a dashed line in Figures 3 and 4. On this plane, and for each time separation τ, the value of spatial separation (shift) ρ_W that corresponded to the maximum of the correlation (crosses in Figure 5a, b) was identified. A value of the velocity was then calculated
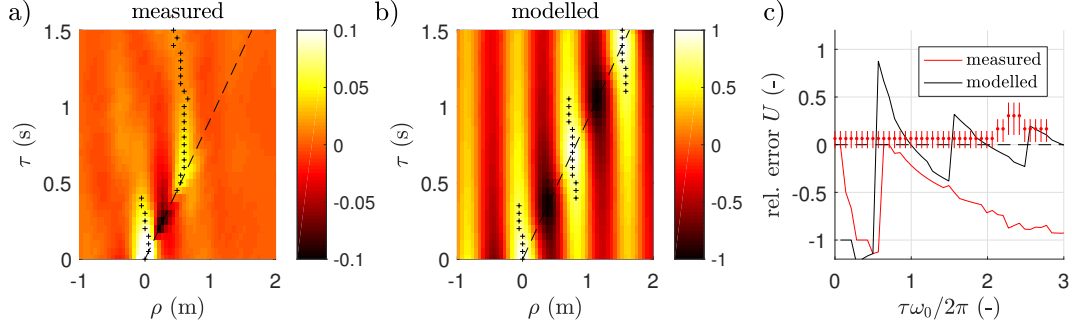
Figure 5. Measured (a) and modelled (b) spatio-temporal correlation on the plane parallel to the flow velocity (dashed line in Figures 3 and 4). (dashed) Expected location of the peak of the correlation assuming rigid advection, $\rho = U\tau$. (crosses) Actual location of the maximum of the correlation, at each time separation τ. (c) Relative error of the velocity measurement, $(U_W - U)/U$, as a function of the ratio between time-lag and characteristic surface period. (solid lines) Velocity estimated from the maxima of the correlation (the crosses in (a), (b)). (red errorbars) Velocity estimated with the suggested technique based on the characteristic spatial period of the correlation.

as $U_W = \rho_W/\tau$. The corresponding relative error, $\varepsilon = (U_W - U)/U$, is shown in Figure 5c as a function of the ratio between the time-lag and the characteristic period, $\tau\omega_0(k_0)/2\pi$, for the measured and modelled correlation.

The correlation functions in Figure 5a, b, show some marked striations with wavelength $2\pi/k_0 = 0.77$ m. The maxima occurred at the crests of these striations, and jumped from stripe to stripe as the time-lag was increased. As a result, the values of ρ_W were effectively quantised, and the error oscillated between $\pm 100\%$ with frequency $\omega_0(k_0)$. This oscillation, and more generally the dependence of the velocity error on the time-lag, appears to be the main effect of the waves on the accuracy. There was some difference between the measured and modelled velocity estimations, especially at low time lags. Here, the model predicted an underestimation by 100 % ($U_W = 0$), while the measurements indicated very little error when τ was small. This difference is believed to be an effect of the rigidly advected features, which were not accounted for by the model. These deformations de-correlate quickly due to their small scale and broad spectrum, but could have been strong enough to ensure that the simplified LSPIV algorithm functioned with reasonable accuracy even in the absence of seeding, if the time-separation was much smaller than the characteristic surface period. This strongly depends on the specifications of the video camera deployed. However, at larger time separations the accuracy decreased rapidly, and the velocity tended to be largely underestimated. This is in agreement with previous LSPIV field observations in unseeded or poorly seeded flows (Tauro et al. 2014, Benetazzo et al. 2017).

Given the lack of control on the characteristic surface period and effective amplitude of the rigidly advected features, LSPIV methods may have limited reliability when the surface is wavy. Techniques to filter out the effects of the waves before (Tani & Fujita 2018) or after (Benetazzo et al. 2017) the calculation of the velocity have been proposed, but they require the ability to at least estimate the actual flow velocity range. Methods that take advantage of the presence of waves in order to infer the statistics of the flow, such as the average velocity, could be more robust. For example, Dolcetti et al. (2018) used the first order statistics of the frequency spectrum measured at a single location, while Dolcetti & García Nava (2019) suggested a fitting of the frequency-wavenumber spectra estimated from measurements at two locations. Here we propose an alternative procedure which applies more directly to video-based measurements of the water surface. The method exploits the periodicity of the correlation function along ρ at each time-lag τ, which is due to the Bessel functions in Equation (14). The characteristic period can be easily identified for any time-lag τ, from the peak of a Fourier transform of $W(\rho, \tau)$ in space. Assuming that such a period approximates $2\pi/k_0$, an estimate of the velocity can be calculated from Equation (5) as

$$U_k = \sqrt{g/k_0}. \tag{15}$$

When applied to the measured data set, the alternative method produced estimates of the velocity that were consistently overestimated by 6.5 %. The overestimation could be due to finite depth and shear effects, which potentially can be addressed (see e.g. Dolcetti et al. 2016). The corresponding

velocity errors are shown in Figure 5c with red dots. The errorbars were calculated considering the uncertainty of the Fourier wavenumber peak location, $\varepsilon_k = 2\pi/L = 1.2$ rad/m, where L is the image size. The velocity estimations were essentially independent of the time-lag up to twice the characteristic period (1.4 s), indicating that the method is robust and can apply potentially to the slow frame rates common in low cost video cameras.

5   CONCLUSIONS

The aim of this study was to detect the presence of gravity waves at the surface of a shallow river from a video collected with a low-cost camera, and to observe their effects on the spatio-temporal correlation of the video frames, in the absence of floating tracers. Gravity waves and rigidly advected features that may correspond to floating tracers or turbulence-generated surface deformations have been identified based on a three-dimensional Fourier analysis of the image intensity collected in videos. Gravity waves with a characteristic wavelength that makes them stationary when propagating directly against the flow have been confirmed to be the dominant pattern at the surface, in accordance with previous studies in the laboratory. A simple analytic model based on a linear superposition of these waves has been used to estimate the shape of the spatio-temporal correlation function, and to compare it with the measurements. The results suggest that some characteristic features of the correlation, such as the periodic change of sign of the correlation peak, and the presence of concentric rings, are due to gravity waves with a characteristic, predictable wavelength.

The potential effect of the gravity waves on the accuracy of LSPIV methods has been investigated based on the use of a simplified LSPIV algorithm. The main effect has been found to be a strong dependence of the accuracy on the time-lag between frames used by the analysis. At time-lags much shorter than the characteristic surface period, the accuracy of the LSPIV algorithm was unaffected. This may be due to the presence of small-scale, rapidly de-correlating features (floats, surface boils, scars, etc.), that moved at the same velocity as the flow. However, the limited frame rate of many low cost cameras, and the larger time-lag employed by most image velocimetry techniques, may be inadequate to cope with such rapidly de-correlating structures. An alternative method to estimate the surface velocity based on the characteristic spatial period of the correlation has been suggested. The velocity estimation error of this method was 6.5 % for the present test, and was independent of the time-lag.

REFERENCES

Benetazzo, A., Gamba, M. & Barbariol, F. (2017). Unseeded large scale PIV measurements corrected for the capillary-gravity wave dynamics. *Rendiconti Lincei* 28(2): 393-404.

Dolcetti, G., Horoshenkov, K. V., Krynkin, A. & Tait, S. J. (2016). Frequency-wavenumber spectrum of the free surface of shallow turbulent flows over a rough boundary. *Physics of Fluids* 28(10): 105105.

Dolcetti, G., Krynkin, A., Horoshenkov, K. V. & Tait, S. J. (2018). An acoustic technique to measure the velocity of shallow turbulent flows remotely. In M. Kalinowska, M. Mrokowska & P. Rowinski (Eds.), *Free Surface Flows and Transport Processes, GeoPlanet: Earth and Planetary Sciences*: 181-194. Cham: Springer.

Dolcetti, G. & García Nava, H. (2019). Wavelet spectral analysis of the free surface of turbulent flows. *Journal of Hydraulic Research* 57(2): 211-226.

Horoshenkov, K. V., Nichols, A., Tait, S. J. & Maximov, G. A. (2013). The pattern of surface waves in a shallow free surface flow. *Journal of Geophysical Research: Earth Surface* 118(3): 1864-1876.

Lubard, S. C., Krimmel, J. E., Thebaud, L. R., Evans, D. D. & Shemdin, O. H. (1980). Optical image and laser slope meter intercomparisons of high-frequency waves. *Journal of Geophysical Research: Oceans* 85(C9): 4996-5002.

Muste, M., Fujita, I. & Hauet, A. (2008). Large-scale particle image velocimetry for measurements in riverine environments. *Water Resources Research* 44(4).

Savelsberg, R. & van de Water, W. (2009). Experiments on free-surface turbulence. *Journal of Fluid Mechanics* 619: 95-125.

Tani, K. & Fujita, I. (2018). Wavenumber-frequency analysis of river surface texture to improve accuracy of image-based velocimetry. In A. Paquier & N. Rivière (Eds.), *River Flow 2018 - Ninth International Conference on Fluvial Hydraulics*. Lyon-Villeurbanne, France, 5-8 September 2018. EDP Sciences.

Tauro, F., Porfiri, M. & Grimaldi, S. (2014). Orienting the camera and firing lasers to enhance large scale particle image velocimetry for streamflow monitoring. *Water Resources Research* 50(9): 7470-7483.